Composites: Part A 143 (2021) 106285

Contents lists available at ScienceDirect

Composites Part A

journal homepage: www.elsevier.com/locate/compositesa

Dynamic behavior of impact hardening elastomer: A flexible projectile material with unique rate-dependent performance

Chunyu Zhao [a], Yu Wang [a], Mingyang Ni [a], Xiaokang He [a], Shouhu Xuan [a,b,*], Xinglong Gong [a,b,*]

[a] CAS Key Laboratory of Mechanical Behavior and Design of Materials, Department of Modern Mechanics, CAS Center for Excellence in Complex System Mechanics, University of Science and Technology of China, Hefei, Anhui 230027, China
[b] State Key Laboratory of Fire Science, University of Science and Technology of China, 96 Jinzhai Road, Hefei, Anhui 230026, China

ARTICLE INFO

Keywords:
Smart materials
Impact behavior
Mechanical properties
Impact hardening effect

ABSTRACT

The impact hardening effect, with mechanical properties strengthened by the impulsive loadings, is a unique phenomenon in certain polymer systems. In this work, the dynamic response of impact hardening elastomer (IHE) composite under different strain rates was studied. Due to the crosslinking interactions between the shear stiffening gel (SSG) and methyl-vinyl silicone rubber (VMQ) in the elastomer structure, the IHE overcomes the cold-flow character by improving the initial storage modulus from 593 Pa to 7260 Pa in the natural state. Besides, the IHE sphere exhibits a typical visco-elastic character under a free dopping rebounding process with a high coefficient of restitution (86.27%) and equivalent modulus (0.18 MPa). Interestingly, another transition between the rubbery and brittle state was verified both experimentally and numerically. Owing to the adjustable mechanical properties according to the different strain rates, the IHE shows a promising perspective as a new generation flexible projectile in non-lethal occasions.

1. Introduction

The impact hardening effect, of which the viscosity or storage modulus can be rapidly increased under applying external loadings, has been found in specific material systems [1–3]. With the excellent performance of energy absorption and stress dissipation [4–7], the impact hardening materials possess great application prospects in the field of personal protections [8–13]. In recent decades, due to the complex social environments, non-military conflicts, and safety requirements for shooting training, it is an emergency task to develop the soft non-lethal projectile. In consideration of the unique self-adapting stiffness of the impact hardening material, it becomes a potential candidate to design non-lethal bullets with controllable impacting levels.

Shear stiffening gel (SSG) is a viscoelastic boronsiloxane polymer with an interesting soft-rigid switching property, which has been extensively studied in recent years [14–16]. Owing to the reversible physical crosslinked B-O (Boron-Oxygen) dynamic bonds in the molecular network, the SSG displays a typical impact hardening effect among the viscous state, rubbery state, and brittle state according to the increment of external strain rates [17–20]. Nevertheless, affected by the inherent cold-flow phenomenon, the SSG cannot retain its original shape in the natural state and needs to be encapsulated within other structures to form a stable shape [21,22], which inevitably increases the design and manufacturing difficulties for the SSG-based materials.

The double network composites, which are generally composed of a rigid-brittle first network and a soft-ductile second network, achieve great improvement on stiffness and toughness compared to the single component materials [23,24]. Inspired by the idea of the double network technique, a new type of impact hardening elastomer (IHE) composite is produced by the physical cross-linked SSG as soft phase and the covalently cross-linked methyl-vinyl silicone rubber (VMQ) as solid phase [25–28]. Due to the interactions between the soft and solid phases, the cold-flow phenomenon is restricted and the IHE keeps a steady shape in the natural state. Besides, inherited from the physical cross-linked B-O bonds in the SSG, the IHE also exhibits a typical impact hardening effect in response to the external impulsive loadings [21,29].

Based on the satisfied structural stability and impact hardening effect, the IHE is an ideal candidate for designing flexible projectiles with adjustable attacking ability. Meanwhile, the brittle property of IHE at a high strain rate can effectively disperse impact energy and reduce the lethality of the projectile. Herein, an IHE composite structure was fabricated by combining the SSG and VMQ *via* a simple mechanical

* Corresponding authors at: CAS Key Laboratory of Mechanical Behavior and Design of Materials, Department of Modern Mechanics, CAS Center for Excellence in Complex System Mechanics, University of Science and Technology of China, Hefei, Anhui 230027, China.
E-mail addresses: xuansh@ustc.edu.cn (S. Xuan), gongxl@ustc.edu.cn (X. Gong).

https://doi.org/10.1016/j.compositesa.2021.106285
Received 15 August 2020; Received in revised form 17 December 2020; Accepted 15 January 2021
Available online 21 January 2021
1359-835X/

stirring method. Firstly, the basic rheological behavior and rate-dependent compression effect were measured using a rheometer system. Secondly, the free dropping rebounding process of an IHE sphere against a rigid surface was analyzed to prove the elastic feature of IHE under the low-velocity impact. Then, the ballistic behaviors of IHE projectile under high-velocity impact were experimentally studied and theoretically discussed. Finally, an impact hardening mechanism for describing the dynamic evolutions of B-O (Boron-Oxygen) bonds was proposed. As a smart projectile with a controllable attacking level and low lethality, the IHE was expected to be a high-performance flexible projectile.

2. Experiment section

2.1. Materials

Boric acid (purchased from Sinopharm Chemical Reagent Co. Ltd, Shanghai, China) and hydroxyl silicone oil (500 mm^2/s, AR degree, purchased from Jining Huakai Resin Co., Ltd) were used to fabricate SSG. Methyl vinyl silicone rubber (VMQ 110-2, purchased from Shenzhen Muwei Technology Co., Ltd.) was the raw material to produce IHE. Benzoyl peroxide (BPO, purchased from Sinopharm Chemical Reagent Co. Ltd, Shanghai, China) was used as the vulcanizing agent in the preparation process.

2.2. Preparation method

Firstly, the boric acid was mixed with hydroxyl silicone oil at the ratio of 50 mg/ml in a ceramic dish through stirring. The mixture was heated at 180 °C for 2 h in an oven (YS20T-S, China). Notably, the mixture was stirred manually for 1 min every 20 min by removing it from the oven to ensure the complete reaction. During the process, the cross-linked polymer formed, and the mixture displayed silky characteristics. Then, by cooling down the mixture to room temperature, the colloidal SSG was obtained (Fig. 1(a)).

Next, the prepared SSG and VMQ were mixed mechanically at a mass ratio of 1:1 in an internal mixer (HL-200, China) at a stirring rate of 45 rpm for 30 min. Meanwhile, the 1.0% w.t. vulcanizing agent BPO was slowly added into the hybrid. After that, the mixture was pressed into a cuboid aluminum mold with the dimension of 60 mm × 60 mm × 2 mm and vulcanized at 100 °C with 20 MPa pressure for 15 min by a plate vulcanization meter (DHG-9036A, China) to ensure the specimens with flat surfaces. Besides, a pair of hemispherical mold with the radius of 12.5 mm and 6.5 mm was utilized respectively to fabricate spherical specimens for free dropping impact testing and high-velocity ballistic impact testing under the same treatment method (Fig. 1(b)). Then, the mixture was removed from the plate vulcanization meter and cooled at room temperature. Finally, the impact hardening elastomer was obtained after the mold releasing process. In this process, the interactions between the SSG and VMQ were generated through the covalent bonding, which could be further proved by the Fourier Transform Infrared Spectroscopy (FTIR) testing (ATR mode from 3500 to 500 cm^{-1}) with the stretching vibrations of Si—O—Si bond (1008 cm^{-1}), Si—O—B (862 cm^{-1}) and B—O bonds (1342 cm^{-1}) (Fig. 1(c)).

2.3. Characterization

The morphologies of IHE were imaged by a digital microscope (Keyence VHX, VH-Z100, Japan). The rheological properties of the IHE were investigated by a rheometer (Physica MCR 302, Anton Paar Co., Austria) with a PP20 parallel plate (Φ20 mm). In the rheological testing, the oscillatory sweeping module was chosen and the frequency swept from 0.1 $rad{\cdot}s^{-1}$ to 100 $rad{\cdot}s^{-1}$ with an amplitude strain of 0.1% at the temperature of 25 °C (ISO 6721–10). Besides, to understand the viscoelastic behavior of IHE, the compression measurement was also implemented using the rheometer system. The specimens were molded into a cylinder of Φ13 mm × 6.0 mm (GB/T 7759.1-2015) and placed between the PP 20 plate and the rheometer base. During the compression process, the strain was controlled by the vertical movement module of the PP20 plate and the compression force was recorded by the normal force sensor in the vertical direction. Based on the relationship between compression stress (σ) and normal force (F) $\sigma = F/\pi r^2$ (r was the radius of the cylinder specimen), the stress–strain curves were obtained. The maximum compression strain was set as 20% and the strain rates are 0.001 s^{-1}, 0.01 s^{-1}, and 0.05 s^{-1}, respectively.

A self-made free dropping impact platform was built to study the low-velocity impact dynamics evolution of the IHE sphere. Through the height-adjustable releasing device attached to a vertical ruler, the IHE

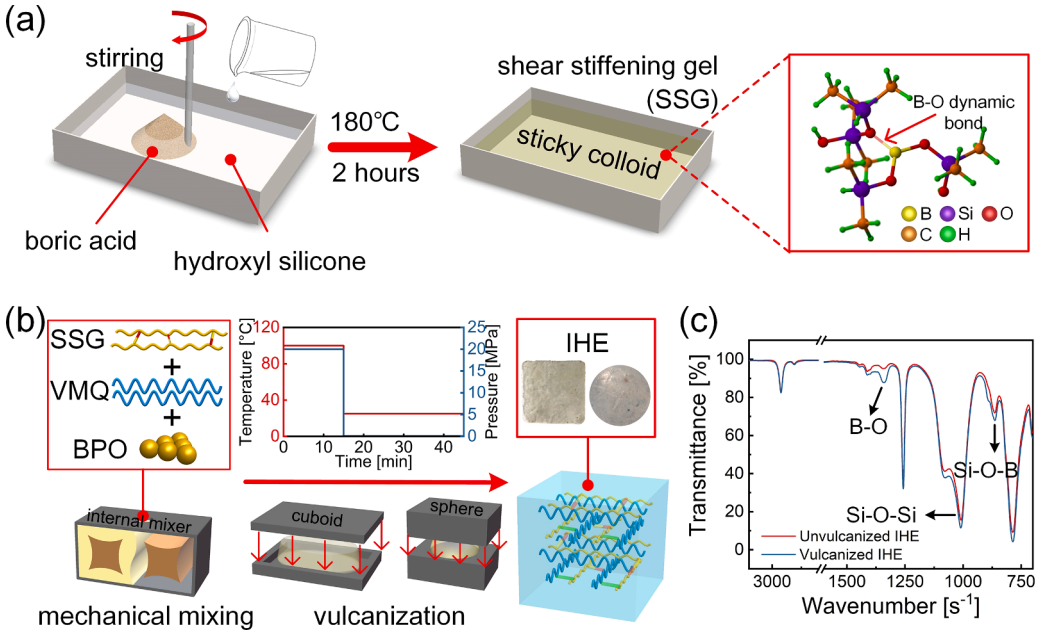

Fig. 1. (a) Schematic of synthetic methods and molecular structure of SSG; (b) Preparation process of IHE based on mechanical mixing method. (c) ATR-FITR spectroscopic characterization of IHE. (For interpretation of the references to colour in this figure legend, the reader is referred to the web version of this article.)

sphere (radius $r_1 = 12.5$ mm) could drop onto the metal plane at the specific heights. The entire rebounding motion was recorded by a digital camera (D7000, Nikon) to measure the coefficient of restitution (COR) and analyze the kinematic behavior. In terms of the contacting process, the high-speed video camera (Phantom v2512, Vision Research Inc.) was used to capture the local deformation of the IHE sphere. Meanwhile, a calibrated piezoelectric film force sensor (H80046, eTouch Inc, China) with a sensitivity coefficient of 50.0 pC/N was located on the impact region to record the impact signals of the IHE sphere and the sampling frequency of the sensor was 625 kHz.

The high-velocity ballistic impact system was consist of a gas gun launcher, targets, and synchronous high-speed video cameras. Driven by the high-pressure gas, the viscoelastic IHE sphere projectile (radius $r_2 =$ 6.5 mm) was endowed with an initial velocity ranging from 30 m/s to 200 m/s. In these experiments, two targets were selected to discover the high-velocity impact behavior of an IHE projectile. As the first one, a PC plate (12 mm × 12 mm × 4 mm) clamped to a steel frame to obtain the local impact evolutions and phase transition details of the IHE impactor. To explore the penetration ability of the IHE sphere within different initial velocities, another target was a ballistic gelatin with the dimension of 100 mm × 80 mm × 50 mm to imitate soft targets such as animal skins and muscular tissues. In the dynamic impact process, a high-speed video camera was placed in the perspective perpendicular to capture the IHE trajectory for calculating the initial velocities and record the axial motion of the IHE projectile. Besides, another camera in the side view synchronously captured the deformation on the contact surface between the IHE and the target.

3. Results and discussions

3.1. Structural stability of the IHE sphere

Firstly, a series of experiments were conducted to illustrate the structural stability of IHE. Compared to the traditional impact hardening materials with typical cold flow behavior, the IHE system showed better formability and long-term stability due to the double network cross-linking between SSG and VMQ in the natural state (Fig. 2(a)). Secondly, a hydrophobic contact angle of over 90° was observed and it illustrated the non-polar interactions between a water droplet and an IHE surface. Therefore, the long term usability in a humid environment could also be guaranteed (Fig. 2(b)). Besides, the polymer structure was able to suspend in the water, which further demonstrated the light-weight nature of IHE (Fig. 2(c)). Last but not least, a novel self-healing ability of IHE was verified. By reconnecting two pieces of IHE in the slide of a catcher at room temperature and pressure for 6 h without extra modifications, the healing process was in-situ recorded by an optical microscope and the rejoined IHE had similar mechanical properties to the original IHE (Fig. S1, See in supplement material S1).

3.2. Basic rheological behavior of IHE

Then, the rheological property of the IHE structure was studied to distinguish the roles of SSG and VMQ in the IHE system. It was found that the storage modulus (G') and loss modulus (G'') of VMQ almost kept a constant value of 7.10×10^4 Pa and 2.32×10^3 Pa in the whole sweeping process, while the SSG showed a typical shear stiffening behavior with the improvement G' ranging from 5.93×10^2 Pa to 2.00×10^5 Pa according to the increasing angular frequency. With the combination of SSG and VMQ, the viscoelastic IHE not only showed a rate-dependent enhancement effect but also improved the initial stability with G' up to 7.26×10^3 Pa (Fig. 3(a)). In this case, the defect of the cold flow phenomenon for the traditional impact hardening materials was effectually solved. Hence, the IHE maintained good formability as a smart flexible matrix in the natural state. Once the frequency exceeded the critical point ($G' = G''$), the SSG started to regulate the overall stiffness of IHE with a dramatically increasing modulus [30]. Besides, this soft-solid transition process was also reversible towards the external stress field. Herein, in consideration of simplifying the preparation technique while maintaining the effective rate-dependent enhancement effect of the material, the mass ratio of SSG and VMQ to prepare IHE was set as 1:1 in this study.

Further, under the quasi-state compression loading and unloading cycle, the strain rate-dependent behavior was also validated. Notably, with the increment of compression strain rate, the maximum stress improved in the loading process. In terms of the unloading process, a hysteresis phenomenon with residual strain was observed at all strain rates. (Fig. 3(b)). During the cycle, the area enveloped by the stress–strain curve represented the energy dissipation density of the IHE sample. The part of the external work was dissipated due to the visco-plastic characteristics of SSG. Simultaneously, the elastic phase of VMQ was responsible for recoverable elastic deformation energy. Besides, a more obvious proportion of plastic deformation energy rate from 34.26% to 49.18% was obtained according to the improvement of strain rate (Fig. 3(c)). Moreover, the secant modulus at the strain of 20% was calculated, and the promotion of modulus with the increasing strain rate further verified the rate-dependent behavior of IHE under low strain rate conditions (Fig. 3(d)). Based on the rheological testing, the components of SSG and VMQ in the IHE system worked synergistically to adjust the mechanical behaviors under different strain rates.

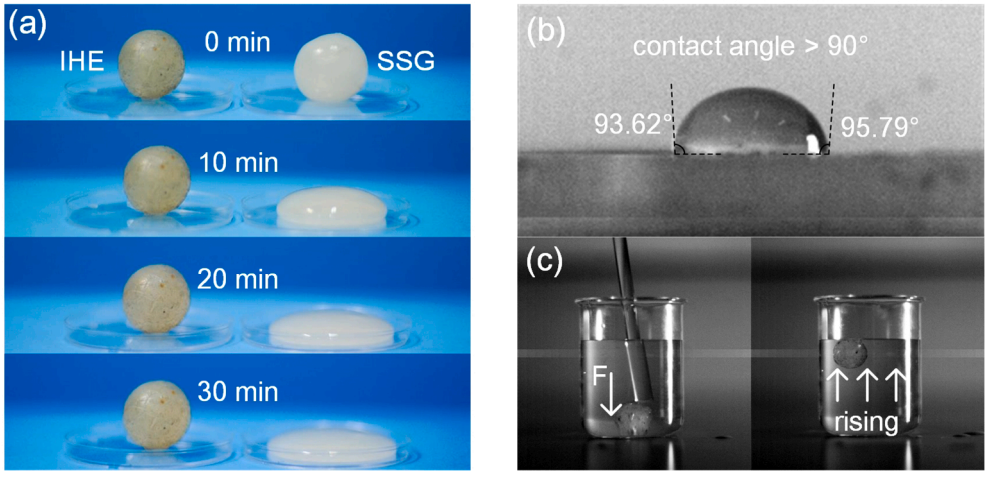

Fig. 2. The structural properties of IHE: (a) Shape stability; (b) Hydrophobicity; (c) Suspension property in water. (For interpretation of the references to colour in this figure legend, the reader is referred to the web version of this article.)

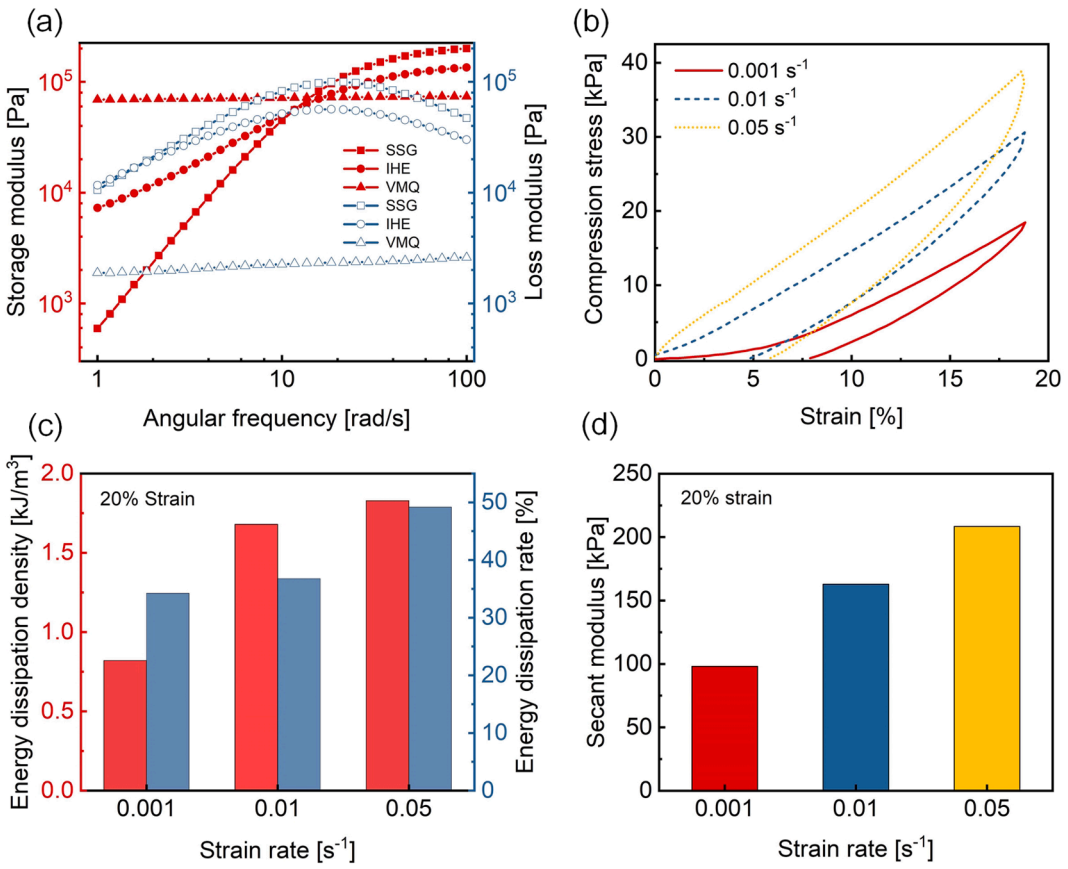

Fig. 3. (a) Rheological properties of SSG, IHE, and VMQ; (b) Low strain rate compression stress *vs* strain curve of IHE; (c) Energy dissipation behavior and (d) Effective secant modulus at 20% strain of IHE during the low strain rate compression loading. (For interpretation of the references to colour in this figure legend, the reader is referred to the web version of this article.)

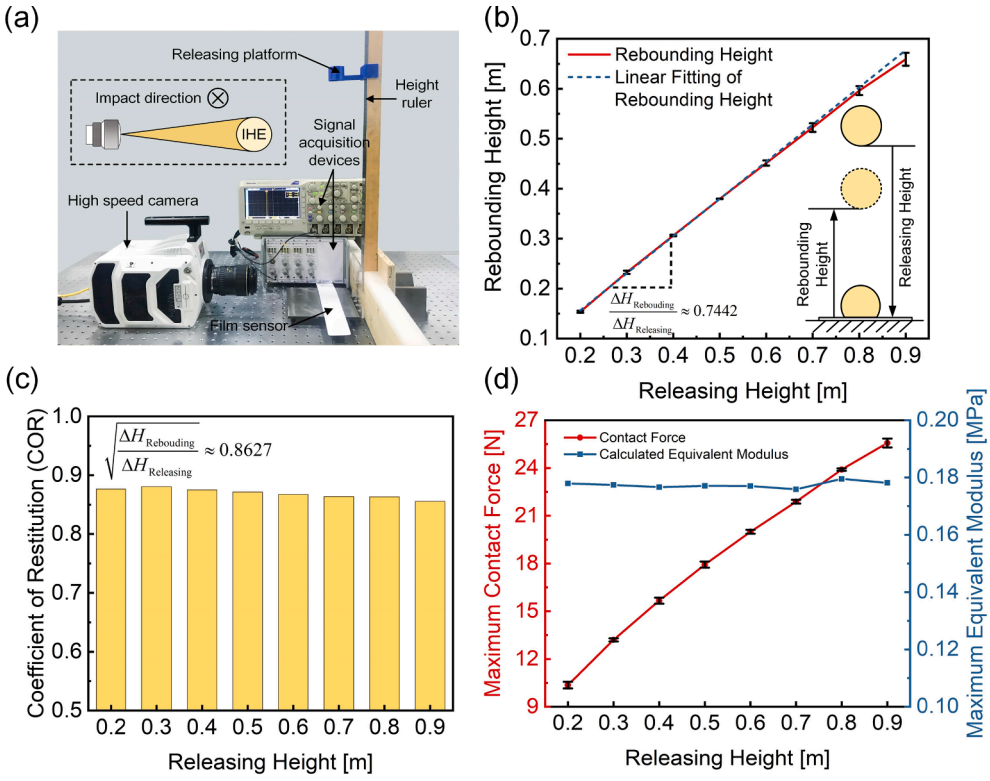

Fig. 4. (a) The experimental configurations of free dropping impact testing system; (b) The kinematic parameters of rebounding height under different releasing height (The inset was the schematic of the IHE free dropping process); (c) The calculated coefficient of restitution (COR) under different releasing height; (d) The dynamics measurement of contact force and the calculation of maximum equivalent modulus during the contact process. (For interpretation of the references to colour in this figure legend, the reader is referred to the web version of this article.)

3.3. Free dropping impact testing of the IHE sphere projectile

To investigate the impact performance of the IHE projectile, the free dropping rebounding process of an IHE sphere was analyzed based on a home-made impact system (Fig. 4(a)). Especially, to ensure the repeatability and reliability of the experiment, three IHE spheres with the same material property were severally released from each of the testing height and the IHE spheres could maintain structural integrity during multiple impact processes (Fig. 4(b)). Firstly, the coefficient of restitution (COR) at different releasing heights was acquired by a digital camera and the IHE sphere exhibited an elastic behavior with high rebounding height. Interestingly, the COR value was almost unchanged at the releasing height ranging from 0.2 m to 0.9 m (Fig. 4(c)). This elastic rate-independent phenomenon corresponded to the elastic plateau region in the rheological curve.

To further verify this conjecture, the equivalent modulus (E_{IHE}) was derived *via* the classical Hertz contact theory (See in supplement material S2). The m, R_{IHE}, and h represented the mass, radius, and the releasing height of the IHE sphere, respectively. In this study, the acceleration of gravity (g) was set as 9.8 m/s^2. The impact force (P) signal was collected by a piezoelectric film sensor. For all of the releasing heights, the Prapidly increased to the peak value (P_{max}) once the IHE impactor contacted the surface. By substituting the P_{max} into Eq. (1), the maximum equivalent modulus ($E_{IHE\text{-}max}$) could be calculated, and the $E_{IHE\text{-}max}$ value was found to be almost a constant at around 0.18 MPa, with the same order of magnitudes as the plateau region in the rheological curve (Fig. 4(d)). Therefore, the IHE sphere in the contact area exhibited complete elastic characteristic, which reasonably explained the invariable COR value for different impact heights.

$$E_{IHE} = \left(\frac{16}{9}\right)^{-\frac{5}{2}} \left(\frac{15mg}{8}\right)^{-\frac{3}{2}} \sqrt{R_{IHE}}\, \frac{P^{\frac{5}{2}}}{h^{\frac{3}{2}}} \quad (1)$$

To better understand the contact details during the rebounding process, the morphology evolutions of an IHE sphere impactor released from the height of 0.6 m were recorded by a high-speed digital camera with a frame rate of 10,000 fps. The entire contact process lasted 3.1 ms and could be divided into four stages based on the contour evolutions extracted by Matlab code based on the pixel recognition of high-speed photography (Fig. 5).

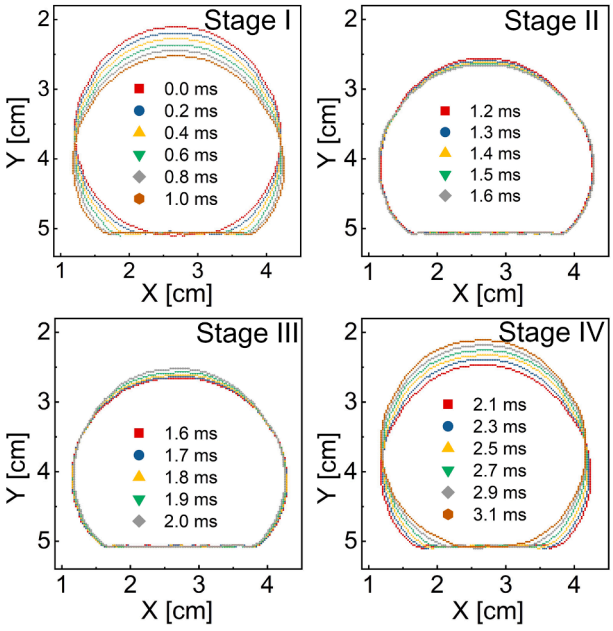

Fig. 5. The contour evolutions of the IHE sphere at the releasing height of 0.6 m during the free dropping impact. (For interpretation of the references to colour in this figure legend, the reader is referred to the web version of this article.)

Stage I (0.1–1.1 ms) represented the loading process after the IHE sphere in contact with the rigid surface. In this stage, the contact stiffness of IHE in the contact region improved with the sudden increase of impact strain rate. However, the contact area still expanded due to the inertial effect of the dropping IHE. Under the circumstances, the top of the IHE sphere compressed downward in the normal direction, while the bottom part expanded horizontally. Stage II (1.2–1.5 ms) appeared once the contact area reached the maximum level. The local high-stiffness elastic property near the contact surface could constrain the deformation at the bottom of the IHE sphere. Meanwhile, a compression trend was still observed on the top of the IHE sphere, which indicated the lower stiffness in the deformation region. In this case, the regional rate-dependent effect during the impact process was further proved. In terms of the unloading section, the stiffness of IHE around the contact region rapidly decreased and the bottom region of the IHE sphere deformed once the unloading process was generated in stage III (1.6–2.0 ms). Moreover, the IHE displayed a more obvious deformation velocity during the initial recovery stage III compared to the loading process in stage II in both the top and bottom part of the IHE sphere (Fig. 6(a), (b)). Finally, the contact area decreased with the sphere rebounding in stage IV (2.1–3.1 ms), which was approximatively symmetrical with stage I.

The experimental results could also be qualitatively compared with finite element analysis (FEA) in ABAQUS/Explicit and the material parameters were obtained through the rheological curve based on the standard linear solid (SLS) model [29]. It was found that the FEA results were in good agreement with the experimental phenomena in terms of contact force, contact time. (Fig. S2, See in supplement material S3). During the rebounding process, the comparison of the experimental results and the FEA simulation results further explained the stiffness distinctions of the IHE sphere during the four deformation stages discussed above (Fig. 6(c)).

3.4. The high-velocity impact response of IHE projectile on a PC plate target

In terms of the high strain rate impact behavior of IHE, the deformation details of an IHE projectile against a 4 mm PC plate target in thickness was investigated based on dynamics methods for the soft impactor structures [31–33] (Movie S1). Similar to the phenomenon of droplets impacting a solid surface in fluid mechanics [34], the IHE exhibited a spreading mode at the beginning of the contact stage owing to the inertial effect. For the projectile with lower initial velocities of 31.12 m/s, the contact region of IHE still maintained a rubbery state as previously discussed in the free dropping impact section. Therefore, obstructed by the elastic force of IHE, the spreading velocity slowed down until the maximum contact area was generated. After this moment, the IHE started to rebound and the elastic force became the driving force, while the inertial force and viscous force were the main resistance. Because of the stiffness degradation effect during the unloading process, the IHE displayed a “pie-straight” rebounding morphology (Fig. 7(a)), showing a certain characteristic of the viscous state. Moreover, the contact process was also simulated through FEA analysis using the same viscoelastic SLS constitutive model in the free dropping test section (See in supplement material S4). The FEA morphology results displayed good consistency with the experimental results which further illustrated the viscoelastic transition of IHE (Fig. 8 (a)).

At a higher initial velocity of 103.73 m/s, the IHE became brittle and a small number of brittle cracks occurred on the contact surface. However, the debris particles were covered due to the inertia effect of the remaining rubbery IHE, and the partial fragmentation could be observed until the rebounding process (Fig. 7(b)). Moreover, a similar impact process was simulated by another “brittle cracking” constitutive relation which further proved the brittle nature of the IHE sphere at ultra-high

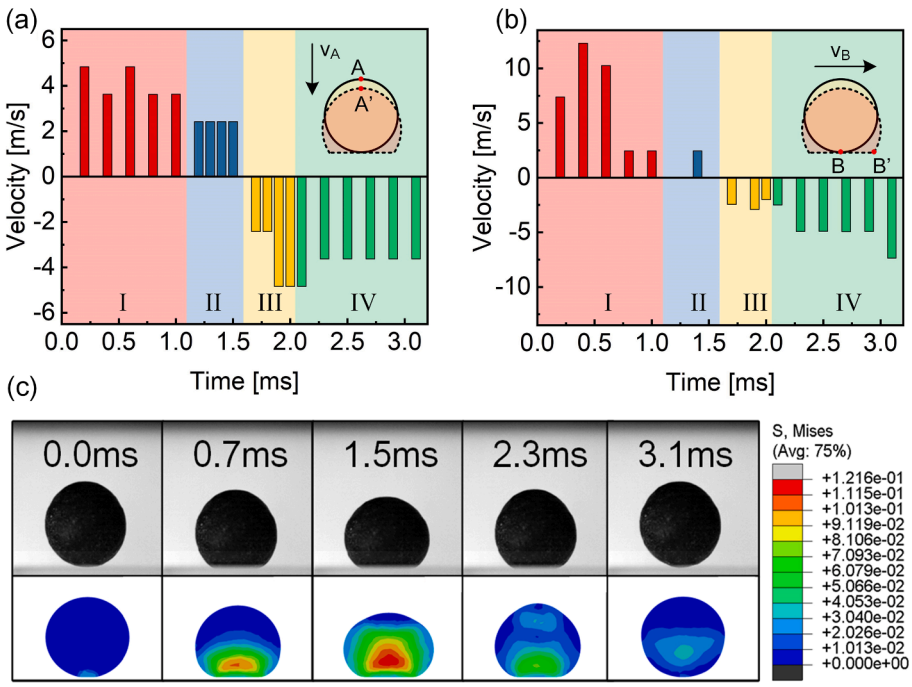

Fig. 6. The velocity of the characteristic point of IHE sphere during the impact process of (a) top part and (b) bottom part at the releasing height of 0.6 m during the free dropping impact; (c) The morphology evolutions of an IHE sphere impactor released from the height of 0.6 m (upper part) and the corresponding FEA results (bottom part). (The surface of the IHE ball was modified with a thin layer of black paint to better identify the sample profile.) (For interpretation of the references to colour in this figure legend, the reader is referred to the web version of this article.)

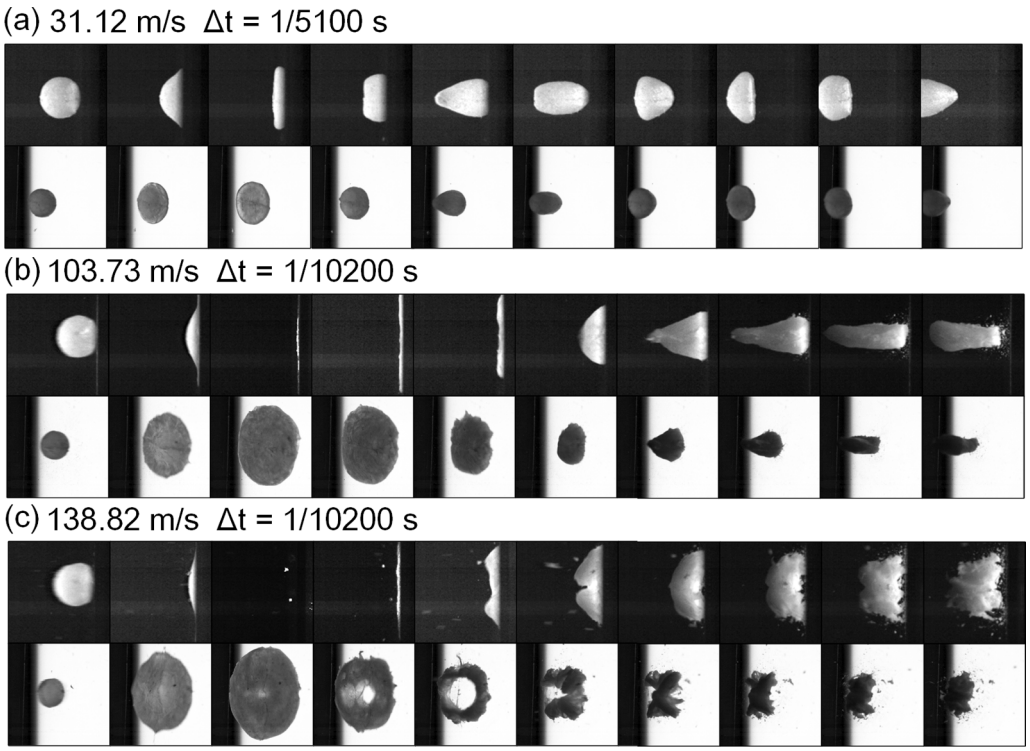

Fig. 7. The impact behavior of IHE projectile in contact with the PC plate: (a) Low-velocity impact; (b) Medium velocity impact; (c) High-velocity impact. (The upper part corresponding to each impact velocity was the perpendicular view to the IHE impact direction, the bottom part was the side view to the PC plate. The initial velocity of the IHE projectile was from left to right in the figure).

strain rate loading (Fig. 8(b)). In this case, another state transition process between the rubbery state and brittle state was certified in the IHE polymer system. With the increasing initial velocity, more regions in the IHE projectile reached the critical strain rate of the brittle state. An astatic "splash" motion was generated among the debris particles once the rebounding process started at the initial velocity of 138.82 m/s (Fig. 7(c)). According to the previous research [35], the penetration threshold energy of human skin under the impact loading of a projectile was a range from 5.8 J to 12.5 J. In this paper, sectional IHE projectile in the contact area started to become brittle once the impact energy reached 5.38 J, while the whole IHE displayed "splash" motions under the impact energy of 9.64 J. In this case, the IHE projectile could prevent it from completely penetrating human skin by a brittle fracture in the range of the threshold energy and effectively reduced the lethality.

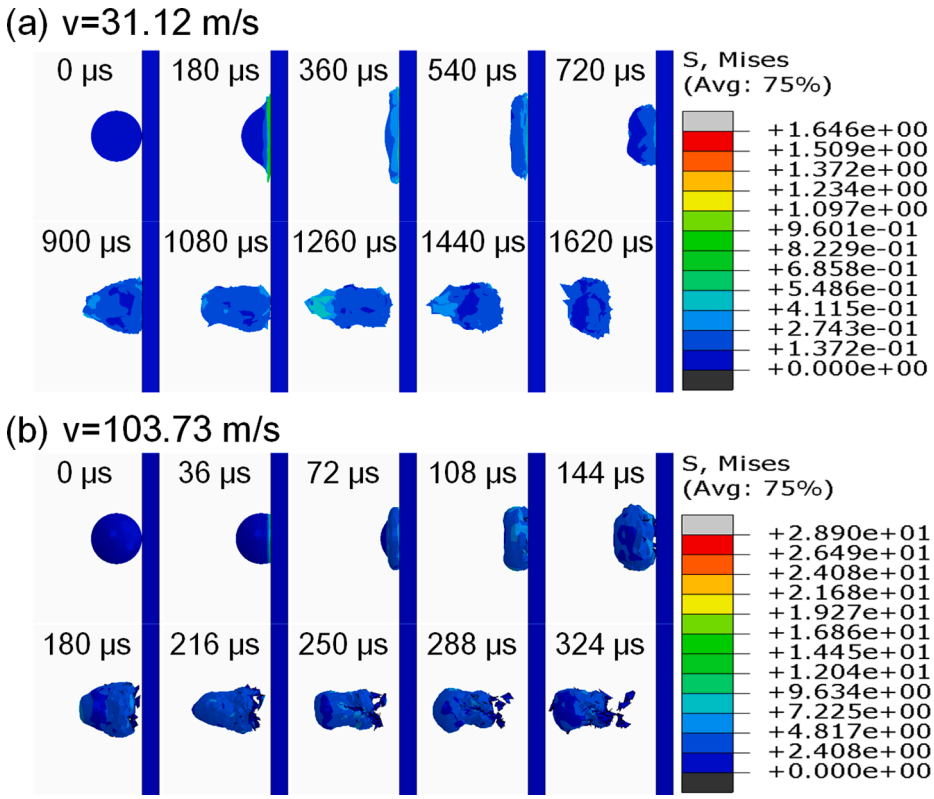

Fig. 8. The FEA morphology evolutions of an IHE projectile in contact with a PC plate at high-velocity impact process: (a) $v = 31.12$m/s; (b) $v = 103.73$m/s. (For interpretation of the references to colour in this figure legend, the reader is referred to the web version of this article.)

3.5. The ballistic behavior between the IHE projectile and the gelatin

In practical applications, the purpose of the non-lethal projectile is mainly focuesd on self-defending and scattering dangerous targets. To simulate the penetration process against the skin tissues with different impact velocities, the contact process between the IHE projectile and ballistic gelatin was recorded according to the previous researches [36,37] based on a ballistic impact testing system (Fig. 9 (a), Fig. S3, See in supplement material S5). During the penetration process, the ballistic line was almost straight and an approximately axisymmetric cavity appeared in the gelatin block (Fig. 9 (b-d)). Due to the existing resistance, the impact velocity of the IHE projectile gradually decreased to zero, while the size of the cavity expanded according to the vertical movement of gelatin (Fig. 10, Movie S2).

In the penetration process, the impact kinetic energy of IHE was mostly converted into the kinetic energy of gelatin moving in the radial direction and the deformation energy of forming the cavity. Notably, in consideration of its tough attribute compared to the soft gelatin, the deformation energy of IHE was small and could be neglected in the later discussions. Based on the cavity motion model [38] (Eq. (2)), the cavity diameter (d) at the gelatin surface and penetration time (t) satisfied the following relationship. Here, the d_m represented the maximum cavity diameter at the gelatin surface. The t_m was the penetration time for the IHE impactor when it decreased to zero. Recorded by the high-speed camera in the perpendicular perspective, the experimental results displayed a good consistency with the cavity motion model, which effectually verified the correctness of the above high-stiff assumption of the IHE impactor in contact with the gelatin at a high strain rate (Fig. 9(e)).

$$d = d_m\sqrt{1-\left[1-\frac{t}{t_m}\right]^2} \tag{2}$$

Inspired by the penetration resistance model [38], the relationships between the penetration depth z(t) and penetration time could be described by Eq. (3). Here, b_1, b_2 were the parameters to be determined, m_s was the mass of the IHE sphere. Based on the z(t) curve recorded by the high-speed camera in the perspective perpendicular to the IHE trajectory, the value of b_1 and b_2 could be accurately fitted (Fig. S4, See in supplement material S5).

$$z(t) = \frac{m_s}{b_1}\left\{ln\frac{cos\left[\frac{\sqrt{b_1 b_2}}{m_s}(t_m - t)\right]}{cos\left[\frac{\sqrt{b_1 b_2}}{m_s}t_m\right]}\right\} \tag{3}$$

Through the change of variable between the penetration velocity v_p(z) (Eq. (4)) and penetration resistance force $F(v_p)$ (Eq. (5)), the penetration resistance force was proved to be a function of penetration depth described by Eq. (6). Where the v_{p0} was the initial velocity of the IHE sphere.

$$v_p(z) = \sqrt{\left(\frac{b_2}{b_1}+v_{p0}^2\right)exp\left(-\frac{2b_1}{m_s}z\right)-\frac{b_2}{b_1}} \tag{4}$$

$$F(v_p) = b_1 v_p^2 + b_2 \tag{5}$$

$$F(z) = b_1\left(\frac{b_2}{b_1}+v_{p0}^2\right)exp\left(-\frac{2b_1}{m_s}z\right) \tag{6}$$

It was demonstrated that the penetration resistance force firstly attenuated quickly and then gently decreased to zero with the penetration of the IHE projectile. The maximum value of penetration resistance force occurred in the initial contact position between the IHE sphere impactor and the gelatin surface and it significantly improved as the increment of the initial velocity of the IHE impactor (Fig. 9(f)). According to the calculation results, the higher penetration force of IHE corresponded to the higher initial velocity, which demonstrated the controllable attacking level of the IHE projectile under different initial velocities. Besides, the geometry of the IHE cavity in the radial direction

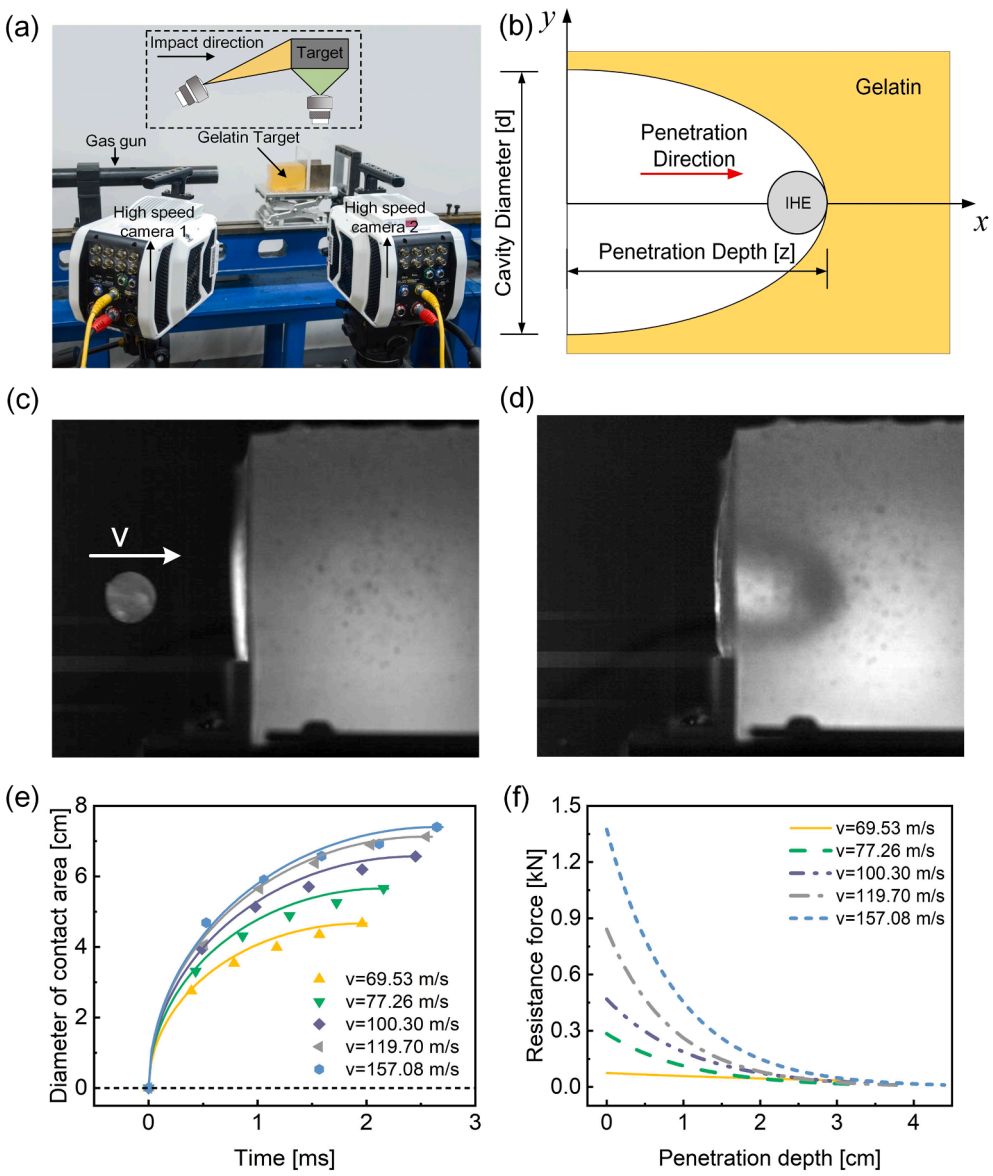

Fig. 9. (a) The experimental configurations of ballistic impact testing system; (b) The coordinate of cavity evolution; (c) The uncontacted state between the IHE projectile and gelatin; (d) The cavity evolution during the penetration process; (e) The evolutions of the diameter of contact area *vs* penetration time (The data points represented the experimental results and the solid lines were the theoretical results based on cavity motion model); (f) The resistance force calculated based on penetration resistance model at different initial impact velocity. (For interpretation of the references to colour in this figure legend, the reader is referred to the web version of this article.)

was proved to be much obvious than that of a solid bullet. In this way, the penetration energy dissipated in the radial direction, and the stress concentration in the axial direction was relieved, which effectively limited the further penetration of IHE. Moreover, the growth of cavity diameter and penetration depth was very small between the initial velocity of 119.70 m/s and 157.08 m/s, and this penetration inhibition behavior could be explained by the rubbery-brittle transition effect corresponding to the abovementioned discussions. In this case, the penetration process against the gelatin target was subdued and the IHE projectile displayed low lethality.

4. Microcosmic mechanism for the rate-dependent effect of IHE

The unique rate-dependent behavior of IHE could be explained by the interactions of crosslinks in the SSG-VMQ double network structure. In this siloxane polymerization system, the weak electron cloud interactions between B and O atoms could be assembled by sharing electrons, which was proved by the stretching vibrations of B—O at 1342 cm^{-1} through Fourier Transform Infrared Spectroscopy (FTIR) techniques. For the unvulcanized IHE, a weak B—O bond absorption peak was observed due to the B—O bond that originally existed in SSG. Interestingly, the more obvious B—O absorption peak after vulcanization corresponded to the formation of cross-linked bonds. Besides, the increasing absorption peak in 1008 cm^{-1} and 862 cm^{-1} also represented the increase of Si—O—Si bonds and Si—O—B bonds during the vulcanization step between SSG and VMQ. In this case, the entanglement of SSG and VMQ in the double network system was responsible for the rate-dependent behavior of IHE.

In terms of low strain rate external loading, the time scale for the polymer disentanglement was much larger than the relaxation time of B—O dynamic crosslinks. The B—O bonds could be broken easily and displayed low stiffness viscous damping nature on the macro-level (Fig. 11(a)). However, due to the existence of other cross bonds between the SSG and VMQ molecular chains, the IHE double network structure still maintained structural stability and deformation recoverability in the natural state. Besides, owing to the good chemical activity of B and O atoms in the healing process, the B—O dynamic bonds could be recombined in the surface of fracture failure, which endowed the IHE with a unique self-healing property. Further, with the increment of the external strain rate, the response time for the molecular motions of IHE became much shorter than the relaxation time of B—O dynamic crosslinks. Under these circumstances, the molecular chains were no longer

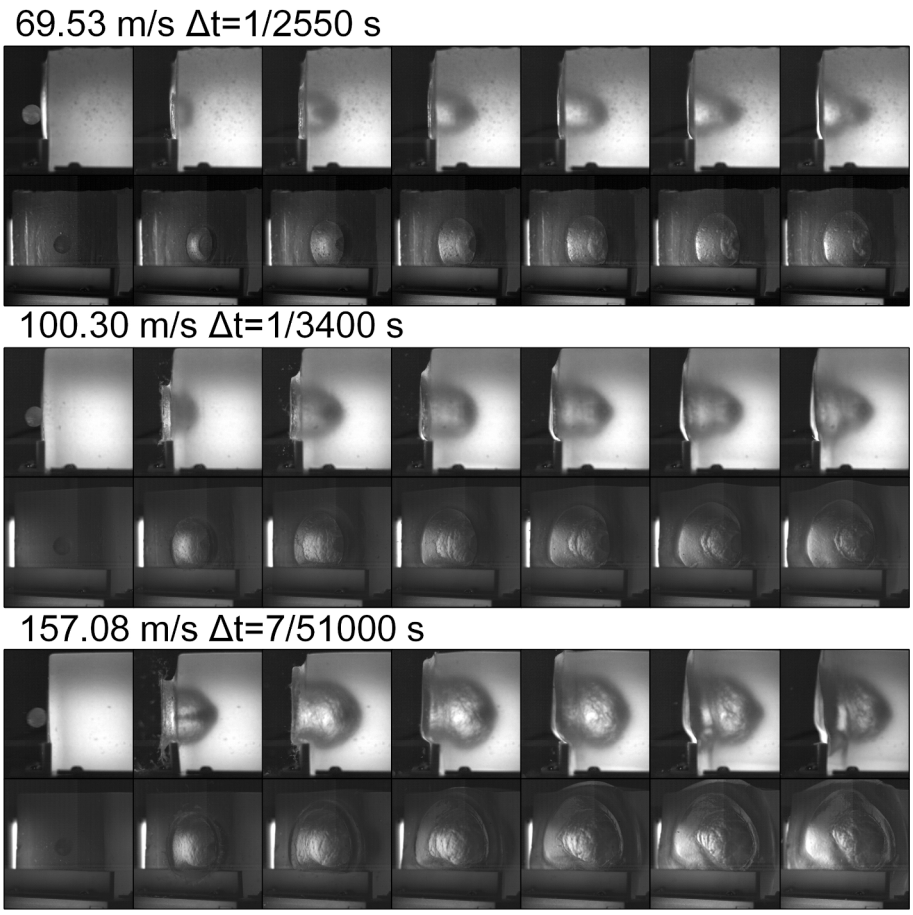

Fig. 10. The cavity evolutions of gelatin under different impact velocities. (The upper part was the perpendicular front view and the bottom part was the side view).

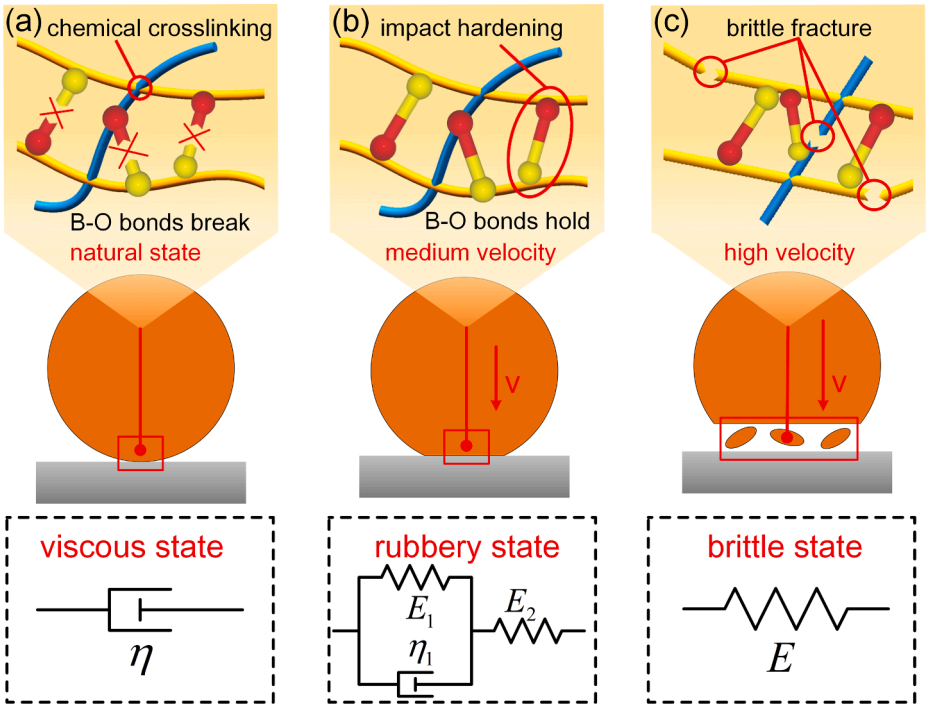

Fig. 11. The mechanism for the unique rate-dependent behavior of IHE under (a) Natural condition; (c) Medium strain rate impact loading and (d) High strain rate impact loading. (For interpretation of the references to colour in this figure legend, the reader is referred to the web version of this article.)

disentangled and the rotation of the chain segments generated greater resistance against the movement of double network molecular chains. Therefore, the IHE showed high stiffness rubbery state at a medium strain rate, which could be explained by the classical SLS model (Fig. 11 (b)). Moreover, once the strain rate continuously increased to a higher level, the response time for all of the cross bonds in the IHE structure was dramatically reduced. Neither breakage of the B—O bonds nor rotation of the polymer chains occurred and the whole double network structure exhibited a crystal lattice structure under hard impacting conditions. The brittle cracking appeared once the external impact load reached the critical value, which was responsible for the elasticity and brittleness of IHE projectile in the ultra-high strain rate loadings (Fig. 11(c)).

5. Conclusion

In conclusion, to discover the suitable materials for designing flexible projectiles, a viscoelastic double network impact hardening elastomer (IHE) composite was prepared. Because of the crosslinks between the SSG and VMQ, the IHE could maintain structural stability in the natural state, which overcame the drawbacks of the cold flow effect for the traditional impact hardening material while maintaining the rate-dependent viscoelastic effect. Besides, the impact testings were conducted to investigate the dynamic response of an IHE projectile within different strain rates. It was illustrated that the IHE projectile exhibited phase transitions among viscous, rubbery, and brittle state. Therefore, the impact level could be controlled according to the variations of impulse loadings, while the brittle characteristic under high strain rate reduced the penetrability and destructiveness of IHE in non-lethal situations. As a high-performance impact hardening material with stretchability, flexibility, strain-rate sensitivity, and shape-recovery ability, the IHE showed high potentials in developing next-generation flexible projectile.

CRediT authorship contribution statement

Chunyu Zhao: Conceptualization, Investigation, Writing - original draft. **Yu Wang:** Methodology, Writing - review & editing. **Mingyang Ni:** Software. **Xiaokang He:** Formal analysis. **Shouhu Xuan:** Writing - review & editing, Funding acquisition. **Xinglong Gong:** Project administration, Funding acquisition.

Declaration of Competing Interest

The authors declare that they have no known competing financial interests or personal relationships that could have appeared to influence the work reported in this paper.

Acknowledgment

Financial supports from the National Natural Science Foundation of China (Grant No. 11972032, 11822209, 11772320, 12072338), and the Strategic Priority Research Program of Chinese Academy of Sciences (Grant No. XDB22040502), the Fundamental Research Funds for the Central Universities (WK2090050045) and Joint Fund of USTC-National Synchrotron Radiation Laboratory (KY2090000055) are gratefully acknowledged. The authors would thank Prof. Erqiang Li of University of Science and Technology of China for his help by supporting the high-speed camera devices.

Appendix A. Supplementary material

Supplementary data to this article can be found online at https://doi.org/10.1016/j.compositesa.2021.106285.

References

[1] Zhang S, Wang S, Wang Y, Fan X, Ding L, Xuan S, et al. Conductive shear thickening gel/polyurethane sponge: A flexible human motion detection sensor with excellent safeguarding performance. Compos Part A-Appl S 2018;112:197–206.
[2] Wagner NJ, Brady JF. Shear thickening in colloidal dispersions. Phys Today 2009;62(10):27–32.
[3] Curosu I, Mechtcherine V, Millon O. Effect of fiber properties and matrix composition on the tensile behavior of strain-hardening cement-based composites (SHCCs) subject to impact loading. Cem Concr Res 2016;82:23–35.
[4] Fu K, Wang H, Zhang Y, Ye L, Escobedo JP, Hazell PJ, et al. Rheological and energy absorption characteristics of a concentrated shear thickening fluid at various temperatures. Int J Impact Eng 2020;139:103525.
[5] Avila AF, de Oliveira AM, Leao SG, Martins MG. Aramid fabric/nano-size dual phase shear thickening fluid composites response to ballistic impact. Compos Part A-Appl S 2018;112:468–74.
[6] Tan Z, Ma H, Zhou H, Han X, Cho C. The influence of graphene on the dynamic mechanical behaviour of shear thickening fluids. Adv Powder Technol 2019;30(10):2416–21.
[7] Cao S, Chen Q, Wang Y, Xuan S, Jiang W, Gong X. High strain-rate dynamic mechanical properties of Kevlar fabrics impregnated with shear thickening fluid. Compos Part A-Appl S 2017;100:161–9.
[8] Gurgen S, Kushan MC, Li W. Shear thickening fluids in protective applications: A review. Prog Polym Sci 2017;75:48–72.
[9] Bai R, Ma Y, Lei Z, Feng Y, Liu C. Energy analysis of fabric impregnated by shear thickening fluid in yarn pullout test. Compos Part B-Eng 2019;174:106901.
[10] Liu K, Cheng C, Zhou L, Zou F, Liang W, Wang M, et al. A shear thickening fluid based impact resistant electrolyte for safe Li-ion batteries. J Power Sources 2019;423:297–304.
[11] Arora S, Majumdar A, Butola BS. Structure induced effectiveness of shear thickening fluid for modulating impact resistance of UHMWPE fabrics. Compos Struct 2019;210:41–8.
[12] Wang Q, Sun R, Yao M, Chen M, Feng Y. The influence of temperature on inter-yarns fictional properties of shear thickening fluids treated Kevlar fabrics. Compos Part A-Appl S 2019;116:46–53.
[13] Gurgen S, Kushan MC. The stab resistance of fabrics impregnated with shear thickening fluids including various particle size of additives. Compos Part A-Appl S 2017;94:50–60.
[14] Jiang W, Gong X, Wang S, Chen Q, Zhou H, Jiang W, et al. Strain rate-induced phase transitions in an impact-hardening polymer composite. Appl Phys Lett 2014;104(12):121915.
[15] Tang M, Wang W, Xu D, Wang Z. Synthesis of structure-controlled polyborosiloxanes and investigation on their viscoelastic response to molecular mass of polydimethylsiloxane triggered by both chemical and physical interactions. Ind Eng Chem Res 2016;55(49):12582–9.
[16] Wang S, Jiang W, Jiang W, Ye F, Mao Y, Xuan S, et al. Multifunctional polymer composite with excellent shear stiffening performance and magnetorheological effect. J Mater Chem C 2014;2(34):7133–40.
[17] Wang Y, Gong X, Xuan S. Study of low-velocity impact response of sandwich panels with shear-thickening gel cores. Smart Mater Struct 2018;27(6):065008.
[18] Zhang D, Jiang N, Chen X, He B. Rheology of crosslinked entangled polymers: Shear stiffening in oscillatory shear. J Appl Polym Sci 2020;137(9):48421.
[19] Zhao C, Wang Y, Cao S, Xuan S, Jiang W, Gong X. Conductive shear thickening gel/Kevlar wearable fabrics: A flexible body armor with mechano-electric coupling ballistic performance. Compos Sci Technol 2019;182:107782.
[20] Wang S, Ding L, Wang Y, Gong X. Multifunctional triboelectric nanogenerator towards impact energy harvesting and safeguards. Nano Energy 2019;59:434–42.
[21] Tang M, Zheng P, Wang K, Qin Y, Jiang Y, Cheng Y, et al. Autonomous self-healing, self-adhesive, highly conductive composites based on a silver-filled polyborosiloxane/polydimethylsiloxane double-network elastomer. J Mater Chem A 2019;7(48):27278–88.
[22] Wu Q, Xiong H, Peng Y, Yang Y, Kang J, Huang G, et al. Highly stretchable and self-healing "solid-liquid" elastomer with strain-rate sensing capability. ACS Appl Mater Inter 2019;11(21):19534–40.
[23] King DR, Okumura T, Takahashi R, Kurokawa T, Gong J. Macroscale double networks: design criteria for optimizing strength and toughness. ACS Appl Mater Inter 2019;11(38):35343–53.
[24] Gong J, Katsuyama Y, Kurokawa T, Osada Y. Double-network hydrogels with extremely high mechanical strength. Adv Mater 2003;15(14):1155–8.
[25] Liu X, Yu K, Fu Q, Qian K. Shear thickening gel reinforced flexible polyurethane foam and its enhanced properties. Smart Mater Struct 2019;28(5):055017.
[26] Martin R, Rekondo A, Ruiz de Luzuriaga A, Santamaria A, Odriozola I. Mixing the immiscible: blends of dynamic polymer networks. RSC Adv 2015;5(23):17514–8.
[27] Yan X, Yang J, Chen F, Zhu L, Tang Z, Qin G, et al. Mechanical properties of gelatin/polyacrylamide/graphene oxide nanocomposite double-network hydrogels. Compos Sci Technol 2018;163:81–8.
[28] Zhang P, Ding X, Wang Y, Gong Y, Zheng K, Chen L, et al. Segregated double network enabled effective electromagnetic shielding composites with extraordinary electrical insulation and thermal conductivity. Compos Part A-Appl S 2019;117:56–64.
[29] Wang Y, Ding L, Zhao C, Wang S, Xuan S, Jiang H, et al. A novel magnetorheological shear-stiffening elastomer with self-healing ability. Compos Sci Technol 2018;168:303–11.

[30] Boland CS, Khan U, Ryan G, Barwich S, Charifou R, Harvey A, et al. Sensitive electromechanical sensors using viscoelastic graphene-polymer nanocomposites. Science 2016;354(6317):1257–60.
[31] Arakawa K, Mada T, Komatsu H, Shimizu T, Satou M, Takehara K, et al. Dynamic deformation behavior of a golf ball during normal impact. Exp Mech 2009;49(4):471–7.
[32] Yang Y, Zeng Q, Wan L. Contact response analysis of vertical impact between elastic sphere and elastic half space. Shock Vib 2018;2018:1802174.
[33] Zhou J, Liu J, Zhang X, Yan Y, Jiang L, Mohagheghian I, et al. Experimental and numerical investigation of high velocity soft impact loading on aircraft materials. Aerosp Sci Technol 2019;90:44–58.
[34] Zhu Y, Liu H, Mu K, Gao P, Ding H, Lu X. Dynamics of drop impact onto a solid sphere: spreading and retraction. J Fluid Mech 2017;824:R3.
[35] Frank M, Peters D, Klemm W, Grossjohann R, Ekkernkamp A, Bockholdt B, et al. Penetrating chest trauma caused by a blank cartridge actuated rubber ball projectile: case presentation and ballistic investigation of an uncommon weapon type. Int J Legal Med 2017;131(5):1307–12.
[36] Jussila J. Preparing ballistic gelatine - review and proposal for a standard method. Forensic Sci Int 2004;141(2–3):91–8.
[37] Kwon J, Subhash G. Compressive strain rate sensitivity of ballistic gelatin. J Biomech 2010;43(3):420–5.
[38] Liu L, Fan Y, Li W, Liu H. Cavity dynamics and drag force of high-speed penetration of rigid spheres into 10wt% gelatin. Int J Impact Eng 2012;50:68–75.